

Received March 13, 2021, accepted April 5, 2021, date of publication April 22, 2021, date of current version May 13, 2021.

Digital Object Identifier 10.1109/ACCESS.2021.3074867

Scan Blindness Free Design of Wideband Wide-Scanning Open-Ended Waveguide Phased Array

XIUYE LIANG^{1,2}, (Student Member, IEEE), ZHE ZHANG^{1,2},
JIANPING ZENG³, (Graduate Student Member, IEEE), FANG GUAN^{3,4},
XIAOHAN LIU^{1,2,3}, AND JIAN ZI^{1,2,3}

¹State Key Laboratory of Surface Physics, Fudan University, Shanghai 200438, China

²Department of Physics, Fudan University, Shanghai 200438, China

³Institute for Nanoelectronic Devices and Quantum Computing, Fudan University, Shanghai 200438, China

⁴Peng Cheng Laboratory, Shenzhen 518000, China

Corresponding author: Fang Guan (fguan@fudan.edu.cn)

This work was supported in part by the China National Key Basic Research Program under Grant 2016YFA0301103, and in part by the National Natural Science Foundation of China under Grant 91750102.

ABSTRACT A wideband wide-scanning open-ended rectangular waveguide phased array in a triangular lattice is presented. Dielectric or metamaterial wide-angle impedance matching superstrates have been widely used in phased arrays to improve the scanning performance. However these dielectric-containing covers cannot solve the problem of scan blindness caused by the surface waves, or even further aggravate the surface wave effect. The modulated surface structures, which consist of the impedance-gradient structures and the surface wave bandgap structures are designed to maximize the wideband wide-scanning performance of the array. The proposed array achieves 40% bandwidth (8-12 GHz), while covering a scanning range of $\pm 65^\circ$ in the E-plane (VSWR < 2.3) and H-plane (VSWR < 2). The practical working frequency band occupies the whole potential operating frequency band between the waveguide TE₁₀ cutoff frequency and the onset frequency of the first grating lobe. An 11 × 11 prototype is fabricated and measured. Good agreement is achieved between the simulated and measured results.

INDEX TERMS Open-ended waveguide, phase array antenna, scan blindness, surface wave bandgap.

I. INTRODUCTION

Phased array antennas, due to their agile scanning beams, are highly desirable in various domains, such as wireless communication systems [1], radio telescopes [2], and radars [3]. In the design of a phased array, its working bandwidth and scanning range are of the prime concerns. Scan blindness has been considered as a critical obstacle to realize wideband wide-angle scanning for phased array antennas [4], [5], because it can occur prior to the incipient grating lobe angle and even appears at an angle not far from broadside. It is observed as the almost total reflections of the input energy in the array feeding ports when steering the beam to particular angles. This phenomenon is associated with the guided modes supported by the array [6]. Under certain Floquet excitations,

The associate editor coordinating the review of this manuscript and approving it for publication was Yanhui Liu¹.

the guided wave mode can be strongly excited, resulting in significant impedance mismatch, thus the array is unable to radiate.

Studies of scan blindness have been conducted in various types of antenna arrays, and began from the experimental observation of unexpected deep nulls in the active element patterns of the rectangular waveguide phased arrays without dielectric covers [7]. In 1968, Farrell and Kuhn [8] predicted the behavior of an element in an infinite phased array of rectangular waveguides by using a modal method of analysis. They observed that the nulls are related to the radiation cancellation of higher order modes in both the waveguide and the external free space. In the same year, Knittel and Oliner [9] investigated the relationship between nulls and possible guided waves for the waveguide end-slot array. At the angle of blindness, the surface waves on the corrugated surface derived from the actual array may

be related to the mechanism that creates a E-plane scan blindness.

The guided wave can also be a surface wave that is supported by a dielectric slab. In 1984, Pozar and Schaubert [5] demonstrated a comprehensive study of infinite dipole array printed on a dielectric substrate. A simple theory, based on coupling from Floquet modes to surface wave modes on the substrate, is shown to predict the occurrence of scan blindness. In the vertical printed dipole array, scan blindnesses were also observed. In 2020, Koo and Nam analyzed the scan blindness in a T-printed dipole array. The main cause of scan blindness was to be a quasi-TEM guided wave mode, which was predicted using the dispersion relation curve obtained from the equivalent circuit [10]. Similar to the dipole array, the microstrip patch array printed on a dielectric substrate is also likely to produce the scan blindness [11].

In 1996, the E-plane scan blindness caused by the TM_z parallel-plate waveguide modes in a single-polarized tapered-slot array was pointed out [12]. In 2008, another type of scan blindness in the single-polarized triangular lattice tapered-slot array which is caused by the half-waveguide mode was identified [13]. In 2014, comprehensive analyses were conducted on the linearly polarized tapered-slot array [14]. Two new types of resonances, namely a parallel-plate cavity mode and a low-order half-waveguide mode were demonstrated to cause scan blindnesses for E-plane scanning.

Along with the mechanism researches for scan blindness, its elimination methods for various kinds of phased arrays have also been proposed [4]. From the fundamental principle, the elimination methods can be divided into two classes roughly, (1) destroy the linear phasing of the guided wave mode or the Floquet mode, and (2) suppress the guided wave mode within the antenna operating frequency band. For the first class, subarraying can eliminate or reduce mismatch due to the scan blindness, but the price paid for this improvement is the arise of the grating lobes [15]. For the second class, metallized cavities have been used in slot arrays [16] and patch arrays [17] to suppress the surface wave in the dielectric substrates. The defected ground structures (DGSs) have been applied to reduce the mutual coupling between array elements and eliminate the scan blindness in microstrip phased arrays [18]. While this method will break the ground plane and may cause strong backward radiation. The electromagnetic bandgap (EBG) structures or metamaterials which can suppress surface waves propagation inside its forbidden bandgap have been used to eliminate scan blindnesses in dipole arrays [19], patch arrays [20] and waveguide end-slot arrays [21]. This is an effective method but only fits for planar printed apertures. Some other parasitic structures also found effective for specific types of antennas, such as the slits and stubs in the T-printed dipole array [10], triangular notches in the tapered-slot antenna array [14] and vias in the probe-fed patch array [11]. However, litter research has been done in modulating the scan blindness in the open-ended waveguide phased array [22].

Apart from the problem of scan blindness, the active input impedance of the unit cell varies significantly versus scanning angle due to the mutual coupling among array elements [23], which usually cause impedance mismatching and dramatically decrease the antenna efficiency at large scan angles. To alleviate this problem, wide-angle impedance matching (WAIM) technology has been employed [24]. It can be realized by the dielectric slabs [9], [25], metasurfaces [26] or metamaterials [27] placed above the phased array aperture, thus improving the wide-scanning performance in the desired frequency band. While these dielectric-containing WAIM covers will further aggravate the surface wave effect, thus deteriorating the scanning performance at high frequencies.

In this paper, we cast our eyes on the open-ended waveguide phased array. Due to the features of simple structure, good reliability and high power handling capability, the waveguide arrays are highly valued for many radar and communication systems. A wideband wide-scanning open-ended rectangular waveguide phased array with modulated surface structures in a triangular grid is proposed. The scan blindnesses in the array without any dielectric covers are displayed clearly in the active reflection coefficient spectrums. Pyramidal dielectric protrusions ($\epsilon_r = 2.2$) are used to overcome the impedance matching deterioration at large scanning angles, especially in the H-plane. While the periodic protruding dielectric structures on the array aperture can also support the surface waves, just like the dielectric slabs. This will further aggravate the influence of the scan blindness effect at high frequencies. Tapered waveguide walls have been found to help construct broad surface wave bandgaps in both E- and H-planes, thus eliminating the scan blindnesses in the desired frequency band. Finally, the pyramidal dielectric structures are combined with the tapered metallic walls to maximize the wideband wide-scanning performance of the open-ended waveguide array. A wideband end-launcher coaxial-to-rectangular waveguide transition is designed to feed each array element. The proposed array can work over a band of 8-12 GHz (40%) when scanning to 65° in the E-plane ($VSWR < 2.3$) and H-plane ($VSWR < 2$). An 11×11 prototype is fabricated and measured to validate our design. The measured and simulated results are in good agreement.

This paper is organized as follows. Section II provides the analysis and design of the infinite open-ended waveguide array, including the radiating element and feeding structure. Section III presents the simulated and measured results of the fabricated 11×11 array prototype. Finally, a brief conclusion is drawn in Section IV.

II. INFINITE ARRAY ANALYSIS AND DESIGN

The configuration of the proposed dielectric-filled metallic open-ended waveguide phased array is illustrated in Fig. 1. The elements are configured in a triangular lattice. The enlarged view of the array element shows the modulated surface structure in detail, which is composed of the pyramidal

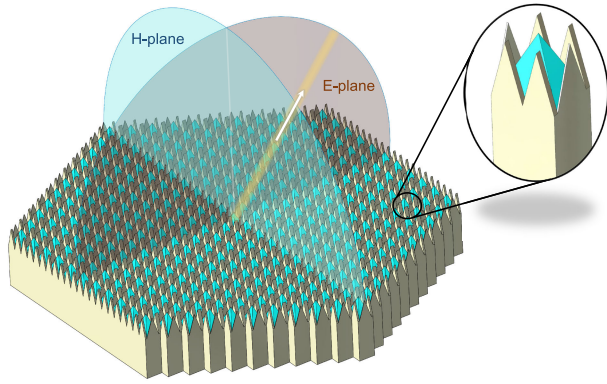


FIGURE 1. Schematic view of the proposed open-ended rectangular waveguide phased array with modulated surface structures.

dielectric protrusion and tapered metallic walls. Each array element is fed by a SMP connector through a in-line coaxial-waveguide transition inside the waveguide, forming a compact configuration. To show the merits of the proposed array, we begin the design from a basic rectangular waveguide array without any covers.

A. BASIC RECTANGULAR WAVEGUIDE ARRAY

For a phased array in the rectangular lattice, the distance between the elements should not exceeding half of the wavelength ($a < \lambda_0/2$) for avoiding the formation of grating lobes at scanning the main beam electronically. Meanwhile, the cutoff wavelength of the fundamental mode (TE₁₀ mode) in a rectangular waveguide is determined by

$$\lambda_{TE_{10}} = 2a_1\sqrt{\epsilon_r}, \tag{1}$$

where a_1 is the long edge width of the rectangular waveguide. To propagate in a rectangular waveguide filled with air, the free-space wavelength of the propagation mode should satisfies $\lambda_0 < \lambda_{TE_{10}} = 2a$, that is $a > \lambda_0/2$. While this contradicts the condition of no grating lobes. In order to overcome this problem the open-ended waveguide is usually filled with the dielectric material with $\epsilon_r > 1$, thus raising the bandwidth by lowering the cutoff frequency of the waveguide fundamental mode. In addition, the triangular lattice is employed to expand the element spacings, thus broadening the waveguide aperture.

Fig. 2(a) shows the lattice arrangement of the proposed array, where a_1 and b_1 is the length and width of the waveguide inner diameters, respectively. The E- and H-plane element spacings are a and b . A larger a_1 is beneficial for reducing the lowest cutoff frequency, while it cannot be too large taking account of the machining of the thin waveguide walls. The open-ended waveguide element fed by a wave port is shown in Fig. 2(b), which is filled with the PTFE materials. The PTFE material is F4BM220 with a relative permittivity of $\epsilon_r = 2.2$ and a dielectric loss tangent of 0.0007. In a two-dimensional infinite array with the triangular lattice, the grating lobes will not appear in the scan region if

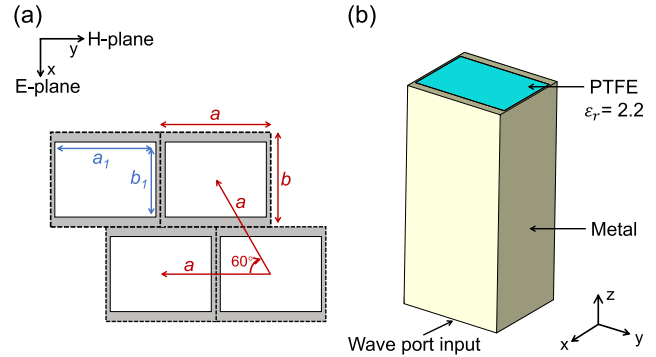


FIGURE 2. (a) The lattice arrangement of the proposed array with key parameters; (b) Topology of the dielectric-filled rectangular waveguide unit cell.

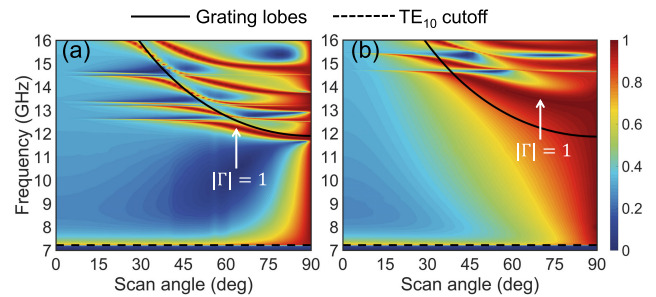


FIGURE 3. Active reflection coefficients $|\Gamma|$ of the proposed array unit cell in an infinite-array environment as a function of frequencies and scan angles. (a) E-plane; (b) H-plane.

the following conditions are satisfied simultaneously [4]:

$$a \leq \frac{1}{\sin \alpha} \frac{\lambda_h}{1 + \sin \theta_{\max}}, \tag{2}$$

$$2b \leq \frac{1}{\cos \alpha} \frac{\lambda_h}{1 + \sin \theta_{\max}}, \tag{3}$$

where θ_{\max} is the maximum scan angle, λ_h is the free-space wavelength corresponding to the highest operating frequency, and $\alpha = 60^\circ$ for the equilateral triangular grid. The structure parameters of the basic rectangular waveguide array are chosen as $\lambda_h = 12$ GHz, $\theta_{\max} = 90^\circ$, $a = 0.58\lambda_h = 14.5$ mm, $b = \sqrt{3}/2a = 12.5$ mm, $a_1 = 0.556\lambda_h = 13.9$ mm, $b_1 = 0.396\lambda_h = 9.9$ mm.

The unit cell shown in Fig. 2 was simulated under periodic boundary conditions using the full-wave simulation software, which can indicate the infinite array performance. Fig. 3 shows plots of the active reflection coefficients $|\Gamma|$ as a function of frequencies and scan angles in the E- and H-planes. Solid black lines are the theoretical onsets of the first grating lobes when scanning in the E- and H-planes. Dashed black lines are the cutoff frequencies of the fundamental mode (TE₁₀ mode) in the rectangular waveguide element. From the reflectance spectrums, the loci of scan blindnesses characterized by $|\Gamma| = 1$ can be identified clearly. It can be seen that a complete scan blindness band occurs before grating lobes enter the visible space only in the E-plane. In addition, the impedance matching for beam scanning in the H-plane is worse than that in the E-plane. These results are consistent

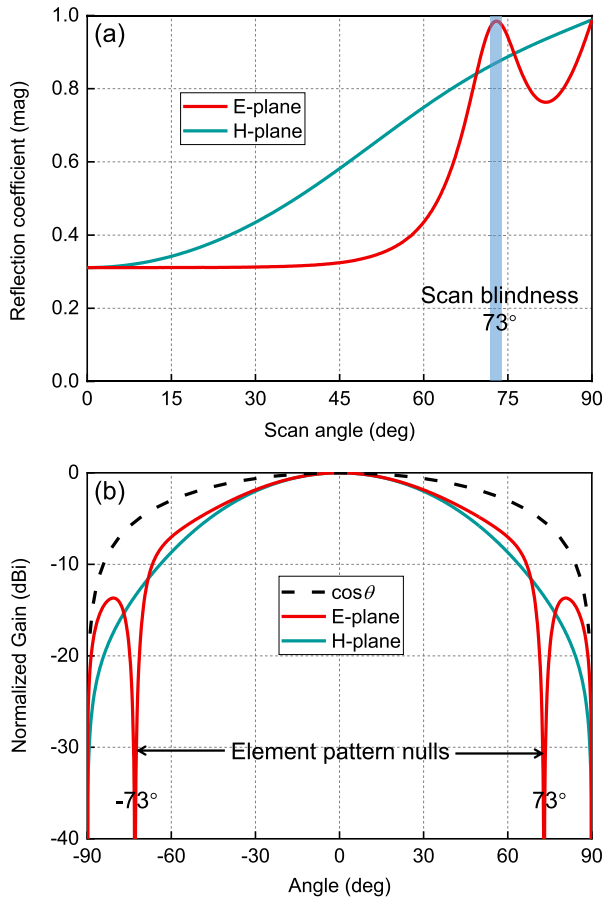


FIGURE 4. Simulated physical images of scan blindness occurrence in the basic rectangular waveguide array. (a) Active reflection coefficients for different scan angles in the E- and H-planes at 12 GHz; (b) Active element patterns in an infinite array (comparison of the E-plane, H-plane and ideal $\cos\theta$ curve).

with previous observations [8]. The surface wave modes on the corrugated array face account for the generation of scan blindness bands [9]. Besides, we find that the scan blindness bands also occur in the H-plane, but they appear after the onset of the first grating lobes. And more scan blindness bands occur at high frequencies in both E- and H-planes, which can be attributed to the high order surface wave modes. Therefore, for the E-plane scan, the main limit is set by the scan blindness rather than by the grating lobes. While for the H-plane scan, the limit is the poor impedance matching for large scan angles.

Fig. 4(a) plots the active reflection coefficients for different scan angles in the E- and H-planes at 12 GHz. The scan blindness can be seen more clearly, which is located at 73° in the E-plane. At this angle, the active reflection coefficient has a peak close to unity. And this will lead to the active element pattern nulls in an infinite array. As seen in Fig. 4(b), the pattern in the E-plane shows deep nulls at $\pm 73^\circ$, which is quite different from the behavior of the H-plane pattern. The ideal $\cos\theta$ curve for an active element pattern is also plotted in Fig. 4(b). For this basic rectangular waveguide array, the beamwidths in both E- and H-planes are much

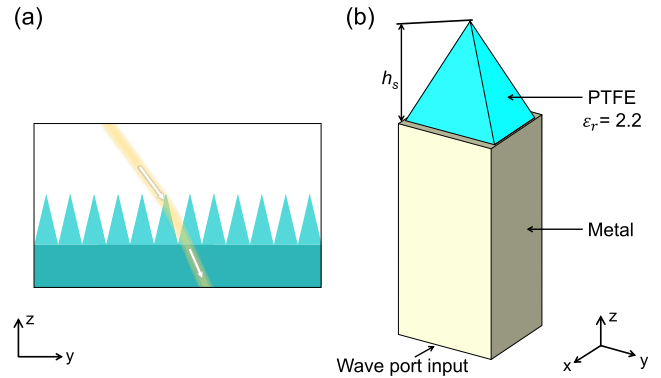


FIGURE 5. (a) Schematic view of the anti-reflection effect in the two-dimensional pyramidal dielectric array surface; (b) Open-ended waveguide unit cell with pyramidal dielectric protrusion.

narrow in comparison with the ideal case, which indicates the high scan losses at large angles.

B. WAVEGUIDE ARRAY WITH IMPEDANCE-GRADIENT STRUCTURES

As shown in Fig. 3(a), good impedance matching can be realized in the E-plane for large scan angles over most of the potential operating frequency band between the TE_{10} cutoff frequency and the onset frequency of the first grating lobe. The most serious problem that needs to be solved is the impedance mismatch for H-plane scan. To address reflections at the aperture-air interface of waveguide phased arrays, dielectric covers [28], [29], protruding-dielectric loadings [30] and metamaterials [27] have been reported to offset the encountered mismatch. In this paper, we use the pyramidal dielectric protrusions to improve the H-plane wide-angle scanning. As shown in Fig. 5(a), two-dimensional (2D) pyramidal dielectric array exhibits homogeneous properties, which can be equivalent to multilayer graded-index slabs [31]. As the impedance-gradient structures, the pyramidal dielectric arrays have been used as wideband wide-angle anti-reflection surfaces in various electromagnetic frequency bands, such as the absorbing structures in microwave anechoic chambers, and anti-reflection coatings in camera lens.

The pyramidal dielectric elements placed on the waveguide array aperture can provide smooth impedance transformation from the waveguide aperture to free-space. Fig. 5(b) shows the open-ended waveguide element with protruding pyramidal dielectric structure, which has the same material as the dielectric filled in the waveguide. Compared with the dielectric slabs covered on the array aperture, the protruding dielectric insertions can make the array structure more compact and offer more design freedom.

Fig. 6 plots the active reflection coefficients $|\Gamma|$ as a function of frequencies and scan angles in the E- and H-planes for different pyramidal dielectric heights h_s . By varying h_s , the H-plane scanning characteristics have been improved, as shown in Fig. 6(d)-(f). But the pyramidal dielectric can only improve the H-plane scanning range at low frequencies. For 10-12 GHz, the active reflection coefficients are still high

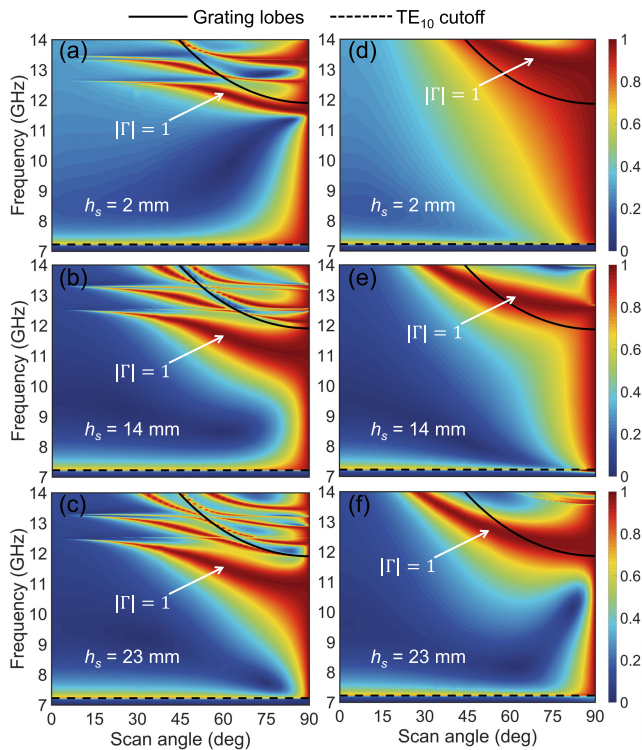


FIGURE 6. Active reflection coefficients $|\Gamma|$ as a function of frequencies and scan angles in the E- and H-planes for different pyramidal dielectric heights h_s . (a)-(c) E-plane; (d)-(f) H-plane. (The results correspond to the array unit cell shown in Fig. 5.)

when scan over 45° in the H-plane due to the influence of the lowest scan blindness band. Besides, we can find that the scan blindness bands in the E-plane move toward lower frequencies as the height h_s increases, thus deteriorating the E-plane scanning performance, as shown in Fig. 6(a)-(c). And the first scan blindness band becomes broader for larger height h_s . Similar behaviour can be observed in the H-plane, where the first scan blindness band appears prior to the first grating lobes for the case of $h_s = 23$ mm. These phenomena are caused by the surface waves which the array can support. The array with protruding dielectric elements is similar to the dielectric-slab covered array, where surface wave modes can propagate along the dielectric slab. And as the thickness of the dielectric increases, the surface wave modes will move to lower frequencies [32].

For the array element shown in Fig. 5(b), the best performance can be obtained when h_s is set around 14 mm. If we use $\pm 60^\circ$ scanning with active VSWR < 2 ($|\Gamma| < 0.33$) as the criteria, the infinite array can realize about 27% bandwidth (7.62-10 GHz) in both E- and H-planes. For the design of wideband wide-scanning open-ended waveguide phased arrays, a dual-polarization circular waveguide array is designed to scan a 60° half-angle cone over a 16% bandwidth [29]. Smolders [28] constructed an X-band rectangular waveguide array with 4096 radiating elements, and 30% bandwidth was achieved when scanning $\pm 60^\circ$ in the E- and H-planes (VSWR < 2). A dielectric sheet combined with

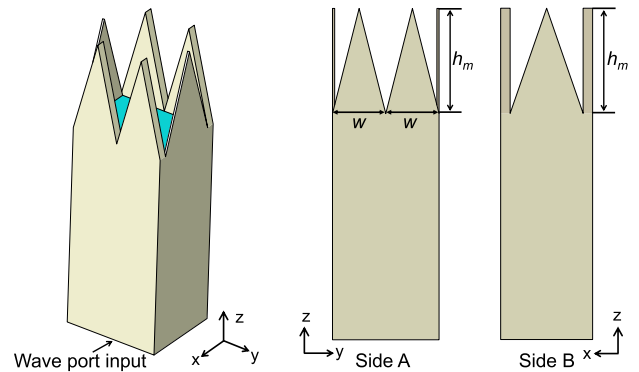


FIGURE 7. Open-ended waveguide unit cell with tapered metallic walls (surface wave bandgap structure).

the metallic iris plate was employed to improve the wideband wide-scanning characteristics. Metamaterial WAIMs have also been studied to obtain better wide angle scanning capability in the circular waveguide phased arrays [27], [33]. Perfect impedance matching can be realized even for $\pm 80^\circ$ scan, but the bandwidth was only shown to be about 18%. To the best of our knowledge, 20%-30% may be the practical bandwidth limit of open-ended waveguide phased arrays by using previously reported WAIM techniques such as irises, dielectric slabs, protruding dielectric insertions and metamaterials.

C. WAVEGUIDE ARRAY WITH SURFACE WAVE BANDGAP STRUCTURES

As described in the previous section, the WAIM layers can only improve the array scanning characteristics over part of the potential operating frequency range (from the TE_{10} cutoff frequency to the onset frequency of the first grating lobe). The obstacle to realizing wider bandwidth, which is the scan blindness band, has not been solved. To address this problem, we proposed an ingenious design to modulate the surface wave bands.

Based on the structure shown in Fig. 2(b), tapered metallic walls are added on the waveguide aperture. There are two pieces of tapered metallic walls on the broad side of the rectangular waveguide (Side A) and one piece tapered metallic wall on the narrow side (Side B), as shown in Fig. 7.

The height h_m of the tapered walls is the key parameter. Fig. 8 plots the active reflection coefficients $|\Gamma|$ as a function of frequencies and scan angles in the E- and H-planes for different heights h_m . Fig. 8(a)-(c) show the reflectance spectrums for the E-plane scan, and Fig. 8(d)-(f) are the H-plane cases. As shown in Fig. 8(a) and (d), scan blindness bands occur at around 10 GHz when $h_m = 8$ mm. When increasing h_m , the scan blindness bands will move toward lower frequencies. For a proper h_m , the lowest scan blindness band can be moved below the cutoff frequency of the TE_{10} mode. In the meantime, the second scan blindness band can be moved above the the onset frequency of the first grating lobe exactly. Thus a complete surface wave bandgap can be constructed between the TE_{10} cutoff frequency and the onset frequency of

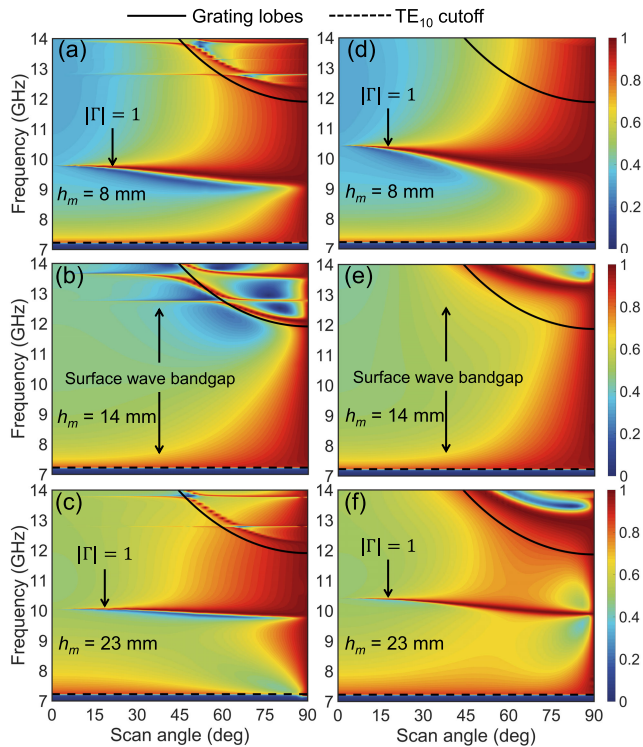


FIGURE 8. Active reflection coefficients $|\Gamma|$ as a function of frequencies and scan angles in the E- and H-planes for different tapered wall heights h_m . (a)-(c) E-plane; (d)-(f) H-plane. (The results correspond to the array unit cell shown in Fig. 7.)

the first grating lobe, as shown in Fig. 8(b) and (e). The height h_m of the tapered metallic walls is crucial to the formation of surface wave bandgaps. As shown in Fig. 8(c) and (f), the second scan blindness band will enter into the operating frequency range if we further increase h_m .

D. WAVEGUIDE ARRAY WITH MODULATED SURFACE STRUCTURES

By using the tapered metallic walls, broad surface wave bandgaps can be constructed in both E- and H-planes, thus effectively removing the scan blindnesses. But it's clear that the impedance matching within the operating frequency band is really bad. Finally, we combined the pyramidal dielectric protrusions with the tapered metallic walls to obtain optimal performance. Fig. 9 shows the final topology of the proposed radiating element with modulated surface structures, which consist of the impedance-gradient structures and the electromagnetic bandgap structures. Fig. 10 presents the active reflection coefficients of the radiating element embedded in an infinite array. The optimal heights are approximately $h_s = h_m = 14$ mm, and the other dimensions keep the same with the basic rectangular waveguide element shown in Fig. 2. Compared with the results shown in Fig. 8(b) and (e), the impedance matching within the surface wave bandgaps is greatly improved, as shown in Fig. 10. The active reflection coefficients are less than 0.33 (VSWR < 2) over 40% bandwidth (8-12 GHz) and more than $\pm 60^\circ$ scan range in both E- and H-planes.

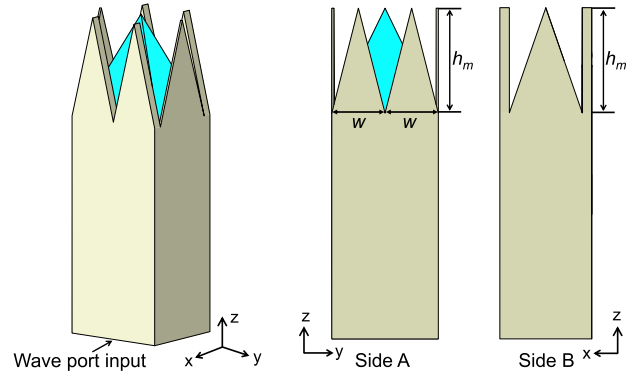


FIGURE 9. Open-ended waveguide unit cell with modulated surface structures, which consist of the pyramidal dielectric protrusion and tapered metallic walls.

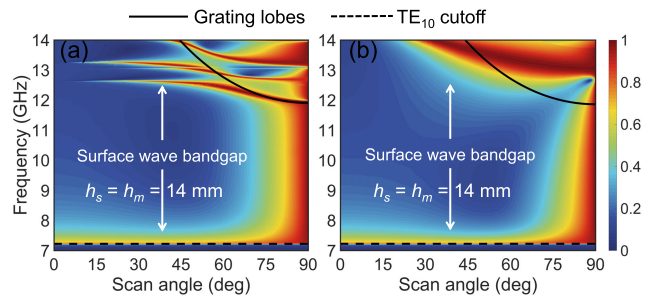


FIGURE 10. Active reflection coefficients $|\Gamma|$ as a function of frequencies and scan angles in the E- and H-planes for the optimal heights ($h_s = h_m = 14$ mm). (a) E-plane; (b) H-plane. (The results correspond to the array unit cell shown in Fig. 9.)

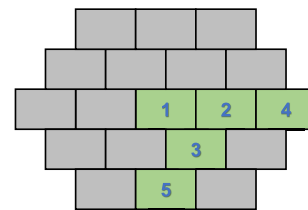


FIGURE 11. Subarray schematic diagram within an 11×11 finite array and the selected ports for S-parameter simulations.

E. MUTUAL COUPLING ANALYSIS

To gain insight to the effect of the tapered metallic walls on mutual coupling, three types of 11×11 finite arrays are simulated: the basic rectangular waveguide array ($h_s = h_m = 0$ mm), the waveguide array with tapered metallic walls ($h_s = 8$ mm; $h_m = 0$ mm), and the waveguide array with both tapered metallic walls and pyramidal dielectric protrusions ($h_s = h_m = 14$ mm). Fig. 11 shows the selected ports for S-parameter simulations. Fig. 12 plots the simulated transmission coefficients of the central port with four adjacent ports.

The yellow curves in Fig. 12(a)-(d) correspond to the case shown in Fig. 8(a) and (b), where there are scan blindness bands at about 9-10 GHz in both E- and H-planes. We can find that there are high humps in four yellow curves at about 9-10 GHz, which indicates that the mutual coupling

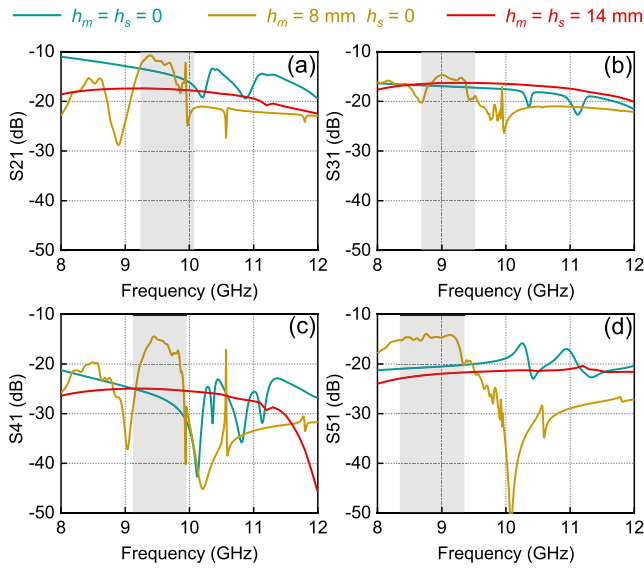


FIGURE 12. Simulated S-parameters for three types of waveguide elements. (a) S21; (b) S31; (c) S41; (d) S51. (The selected ports are shown in Fig. 11.)

between the elements is strong when scan blindness occurs. The red curves in Fig. 12(a)-(d) correspond to the case shown in Fig. 10, where there are board surface wave bandgaps during the desired frequency band in both E- and H-planes. In this case, the humps disappear and the mutual coupling has been reduced. These comparisons show that proper height of the tapered metallic walls can reduce the mutual coupling and eliminate the surface waves. The cyan curves in Fig. 12(a)-(d) correspond to the case shown in Fig. 3. In this case, the scan blindness bands are at the edge of the frequency band, thus the mutual coupling strength keeps the similar level with that of the red curves on the whole. In addition, compared with the cyan and yellow curves, the red curves are much flatter, which means that the dielectric protrusions combined with tapered metallic walls at proper height can make the array performance more stable over a wide frequency band.

F. SQUARE WAVEGUIDE ARRAY IN THE SQUARE LATTICE

To prove the universality of our proposed design method, the square waveguide array in a square lattice is also analyzed. Fig. 13(a) shows the lattice arrangement of the square waveguide array, where a_1 is the length of the waveguide inner diameters. The E- and H-plane element spacings are both a . Fig. 13(b) shows the unit cell with both pyramidal dielectric protrusion and tapered metallic walls. The height of the tapered metallic walls is h_m , and the height of the pyramidal dielectric protrusion is h_s . The basic structure parameters are chosen as $\lambda_h = 12$ GHz, $\theta_{max} = 90^\circ$, $a = 0.5\lambda_h = 12.5$ mm, $a_1 = 0.468\lambda_h = 11.7$ mm. The thickness of the waveguide walls is 0.8 mm.

Fig. 14(a) and (b) plots the active reflection coefficients $|\Gamma|$ in the E- and H-planes for the basic square waveguide array structure ($h_s = h_m = 0$). Similar to the triangular lattice

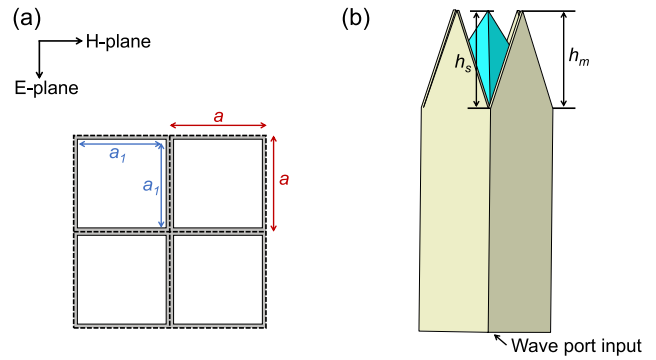


FIGURE 13. (a) The square lattice arrangement of the square waveguide array with key parameters; (b) Topology of the square waveguide unit cell with both pyramidal dielectric protrusion and tapered metallic walls.

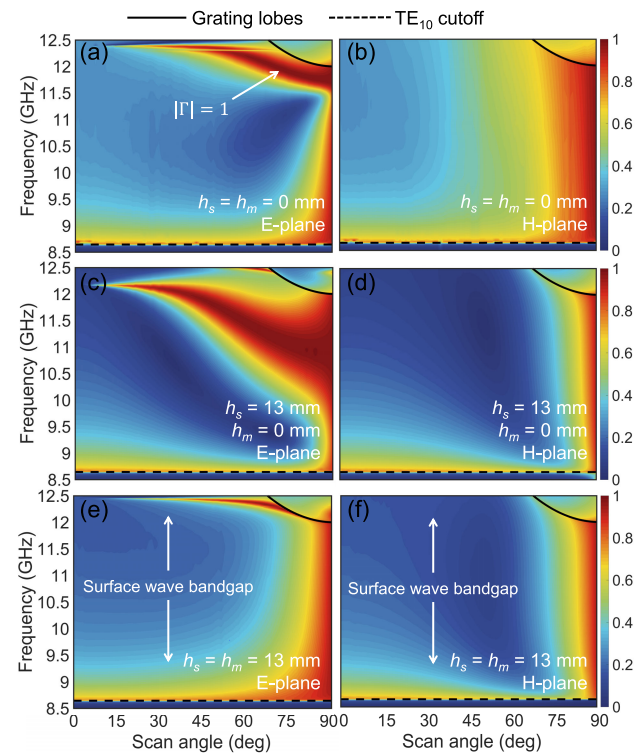


FIGURE 14. Active reflection coefficients $|\Gamma|$ as a function of frequencies and scan angles in the E- and H-planes for three types of waveguide elements. (a)-(b) $h_s = h_m = 0$; (c)-(d) $h_s = 13$ mm, $h_m = 0$; (e)-(f) $h_s = h_m = 13$ mm.

arrangement case, good impedance matching can be realized in the E-plane for large scan angles over most of the potential operating frequency band between the TE_{10} cutoff frequency and the onset frequency of the first grating lobe. A complete scan blindness band occurs before grating lobes enter the visible space in the E-plane. The impedance matching in the H-plane is poor.

Fig. 14(c) and (d) plots the active reflection coefficients $|\Gamma|$ in the E- and H-planes for the square waveguide array with only pyramidal dielectric protrusions ($h_s = 13$ mm, $h_m = 0$). The impedance-gradient structures improve the H-plane scanning performance significantly, while the influence of

the surface wave effect in the E-plane has been further aggravated. Fig. 14(e) and (f) plots the active reflection coefficients $|\Gamma|$ in the E- and H-planes for the square waveguide array with both pyramidal dielectric protrusions and tapered metallic walls, the optimal heights are approximately $h_s = h_m = 13$ mm. Broad surface wave bandgaps are constructed in both E- and H-planes between the TE_{10} cutoff frequency and the onset frequency of the first grating lobe. In addition, good impedance matching is obtained during the desired frequency band. Finally, the active reflection coefficients are less than 0.33 (VSWR < 2) over about 25% bandwidth and more than $\pm 60^\circ$ scan range in both E- and H-planes. Compared with the triangular lattice array, this square lattice array has a relatively narrow bandwidth due to the higher TE_{10} cutoff frequency. But the square array has symmetrical structure and can be extended to a circularly polarized configuration easily.

The above results prove that our design method is effective for both the triangular lattice arrangement and the square lattice arrangement. From the results of above two cases, some valuable design guidelines can be summarized. The pyramidal dielectric protrusion can be considered as a multi-section impedance transformer. Under the condition of taking no account of the scanning blindness, the bandwidth of the pyramidal dielectric protrusion increases with the dielectric height h_s . We need to achieve the desired bandwidth using the lowest height h_s . The tapered metallic walls are utilized to construct surface wave bandgaps by adjusting the locations of the surface wave bands. The scan blindness will appear when the wave vector of surface wave mode matches that of the Floquet mode, thus the frequency of the scan blindness can be adjusted by modulating the wave vector of the surface wave. Changing the height of the metallic walls is essentially adjusting the wave vectors of the surface wave modes on the array aperture. In both cases, the optimal heights of the dielectric protrusions and metallic walls are both about half wavelength corresponding to the highest working frequency. This conclusion will facilitate the design of this kind of antenna array.

G. FEEDING STRUCTURE

To practically implement a waveguide phased array, the feeding network is also critical. In the section, the feeding structures are designed for the rectangular waveguide array. We need a coaxial-to-rectangular waveguide transition with more than 40% bandwidth. Due to the limited space behind each radiating element, end-launcher transition configuration is preferred [34]. Mode conversion theories and impedance matching techniques can provide guidelines to the fast design of the transition. The final topology of the radiating element with feeding network is shown in Fig. 15, which includes five sections, 50 Ω coaxial input, mode conversion section, impedance transformer, rectangular waveguide, and modulated surface structures. The ridge adapter and stepped ridges are made of metal. Taking account of the processing and assembling, section B is filled with air, and sections C and D are filled with PTFE materials.

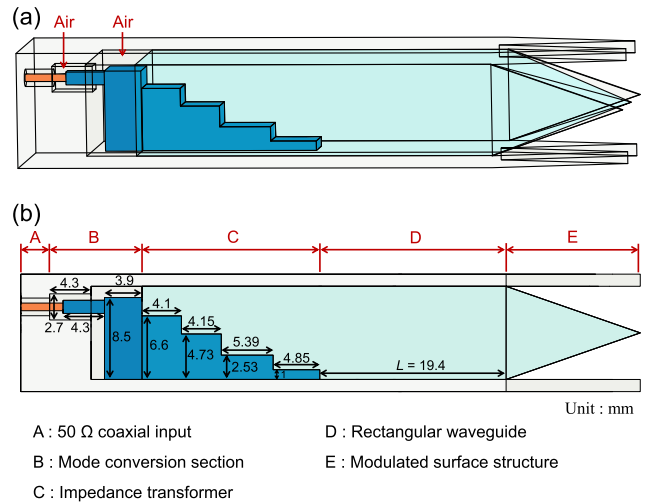


FIGURE 15. Final topology of the proposed array unit cell with feeding network. (a) Oblique view; (b) Side view with detailed dimensions.

The design was carried out in a sectional manner. There are two problems need to be considered, one is the mode conversion from TEM mode in coaxial line to TE mode in waveguide, and the other is the impedance matching between the high impedance of waveguide and low impedance of coaxial line. Section A can be realized by a SMP connector. The mode conversion section (Section B) consists of two parts. The first part is made up of the inner conductors of the circular coaxial line and the square coaxial line, which converts the TEM mode in the circular coaxial line to the TEM mode in the square coaxial line. The second part is a ridge adapter linking the square coaxial line to a ridge waveguide, thus making the TEM mode in the square coaxial line convert to the TE_{10} mode in the single-ridge rectangular waveguide smoothly.

Stepped ridges in the waveguide can be used to accomplish the impedance transformation. In view of the size and bandwidth, a fourth-order Chebyshev type of impedance transformer is included. There are three kinds of characteristic impedance definitions for the ridge waveguide, the Z_{PV} (ratio of power and voltage), Z_{VI} (ratio of voltage and current), and Z_{PI} (ratio of power and current). For the transmission lines with large changes in the cross sections, selection of voltage integration lines for each part cannot be standardized. Hence, Z_{PI} is chosen in this design. The impedance Z_{PI} of a single-ridge waveguide can be estimated by empirical relations [34]. We used the full-wave electromagnetic simulation software to obtain the relation between the impedance and the ridge height.

Finally, the feeding network combined with the radiating element was optimized in the infinite-array environment. The detailed dimensions are presented in Fig. 15(b). Fig. 16 plots the variation of impedance with frequency for each step. As can be seen, the average impedance of each step is reduced from around 450 Ω to around 50 Ω gradually. Fig. 17 presents the simulated active VSWR of the final configuration shown in Fig. 15. As can be seen, the active VSWR of the proposed

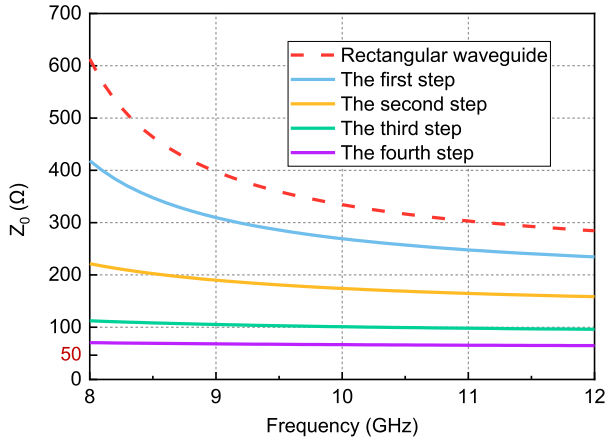


FIGURE 16. Variation of characteristic impedance of each step in the feeding network with frequency.

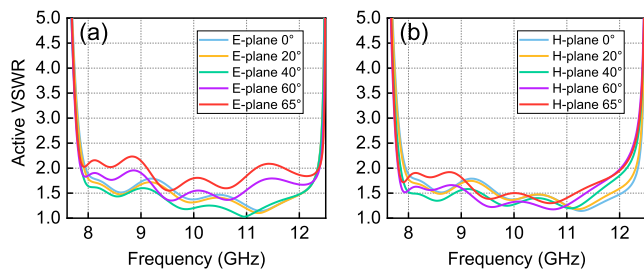


FIGURE 17. Simulated active VSWR of proposed array in the E- and H-planes at five different scanning angles. (a) E-plane; (b) H-plane.

infinite array maintains < 2.3 when scanning up to 65° in the E-plane, and maintains < 2 when scanning up to 65° in the H-plane within 40% bandwidth (8-12 GHz).

III. PROTOTYPE FABRICATION AND MEASUREMENT

To experimentally verify the design of the proposed array, an 11×11 rectangular waveguide array was fabricated and measured. The measurement setup is shown in Fig. 18(a), and the fabricated prototype is shown in Fig. 18(b). The overall dimensions of the proposed array are $19.5 \text{ cm} \times 19.5 \text{ cm} \times 6.5 \text{ cm}$. The radiation patterns of the central element within the array are simulated and measured when other elements are loaded with 50Ω matching loads.

To evaluate the impedance matching results of the array, the active VSWR measurements of the central element were conducted using an Agilent vector network analyzer. The reflection and transmission coefficients of the central element with all other surrounding elements were collected, while all other ports are matched to 50Ω . The active VSWR of an element (p, q) within an array can be expressed as

$$\Gamma_{pq}(\phi_0, \theta_0) = \sum_{m=1}^M \sum_{n=1}^N S_{pq,mn} e^{-j\vec{r}_{mn} \cdot (\hat{x}u_0 + \hat{y}v_0)}, \quad (4)$$

where (ϕ_0, θ_0) is the array scan direction; $S_{pq,mn}$ are the S-parameters between elements pq and mn ; k_0 is the free space wavenumber; $u_0 = k_0 \sin \theta_0 \cos \phi_0$, $v_0 = k_0 \sin \theta_0 \sin \phi_0$ are the $u-v$ coordinates; M, N are the number

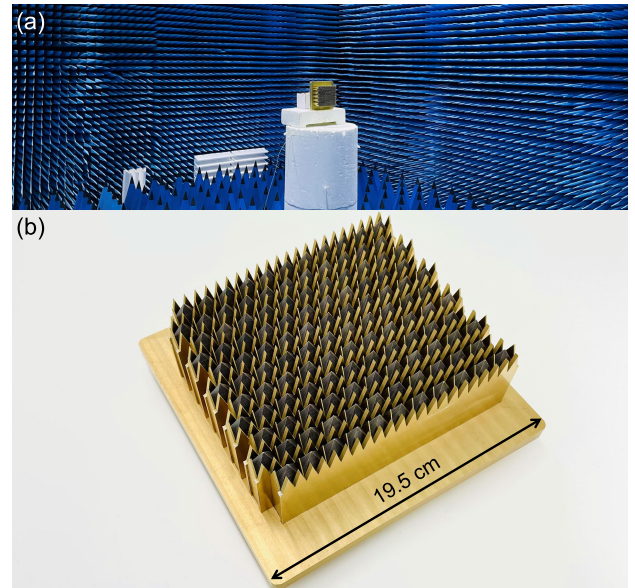


FIGURE 18. (a) Measurement setup and environment; (b) Fabricated 11×11 prototype.

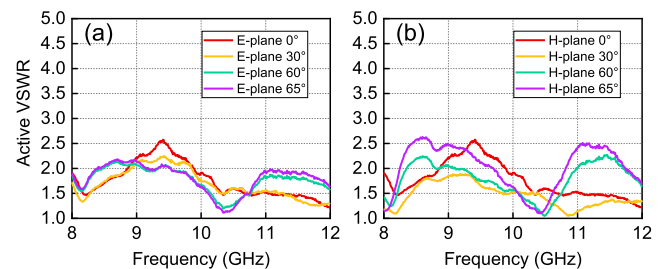


FIGURE 19. Measured active VSWR of the array prototype in the E- and H-planes at four different scanning angles. (a) E-plane; (b) H-plane.

of elements; and \vec{r}_{mn} is the coordinate position vector of element mn . The measured active VSWR of the central element under various scanning angles is shown in Fig. 19. It can be found that there is no scan blindness over the whole operating band. The measured active VSWR is comparable to the simulated ones shown in Fig. 17, though with two higher humps. The slight discrepancy can be attributed to the truncation effect and the testing errors.

Fig. 20 shows the measured and simulated embedded element radiation patterns of selected frequencies in two principal scan planes, including 8 GHz, 10 GHz, 12 GHz. Measured and simulated co-polarized patterns are in good agreement. The cross-polarization performance of the embedded element is superior, which is more than 30 dB below the co-polarization on average out to 60° for all planes. Cross-polarization in the H-plane is too low to be measured in the anechoic chamber. The measured cross-polarization levels in the H-plane are a little higher than the simulated results but still remain low levels. The embedded element patterns have relatively good symmetry. Small ripples varied within 2 dB can be observed in the measured co-polarized patterns, which are mainly due to the small, finite size of

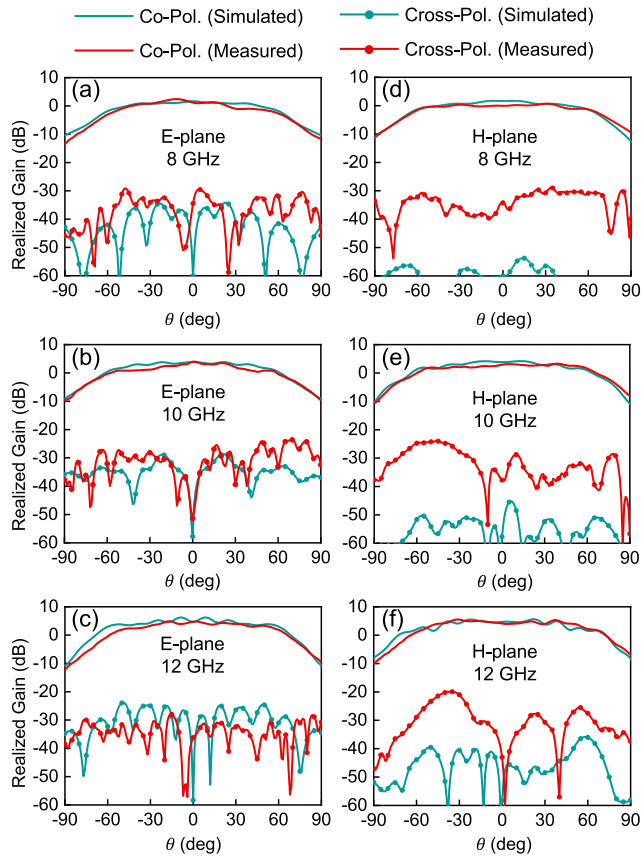


FIGURE 20. Comparisons of measured and simulated embedded element patterns for the central element in the proposed array. (a) E-plane @ 8 GHz; (b) E-plane @ 10 GHz; (c) E-plane @ 12 GHz; (d) H-plane @ 8 GHz; (e) H-plane @ 10 GHz; (f) H-plane @ 12 GHz.

the array and will decrease as the array size increases. The embedded element patterns in the E- and H-planes at different frequencies have wider 3 dB beamwidths, compared with the active element patterns of the basic rectangular waveguide array shown in Fig. 4(b). Thus the modulated surface structures can also widen the beamwidths of the active element patterns effectively, which indicates the wide angle scanning capability of the array.

Fig. 21 plots the measured and simulated radiation patterns at 8 GHz, 10 GHz and 12 GHz for the scan at broadside, 15°, 30°, 45°, 60°, 65° in the E- and H-planes. The measurement was conducted following the unit excitation active element pattern method [35]. Apparently, the measured scanning radiation patterns demonstrated good agreement with the simulated ones of the finite array. The proposed array displayed the ability to scan up to more than 60° in two principal planes. It is worth noting that the maximum scanning angles of the proposed array can only reach about 58° and 62° when scanning to 60° and 65°, respectively. This beam pointing deviation effect for large scan angles will be alleviated when the array size is large enough. In all scan cases, the sidelobes are well below -11 dB.

The measured realized gains versus frequency at broadside and 60° scan in the E- and H-planes are plotted in Fig. 22,

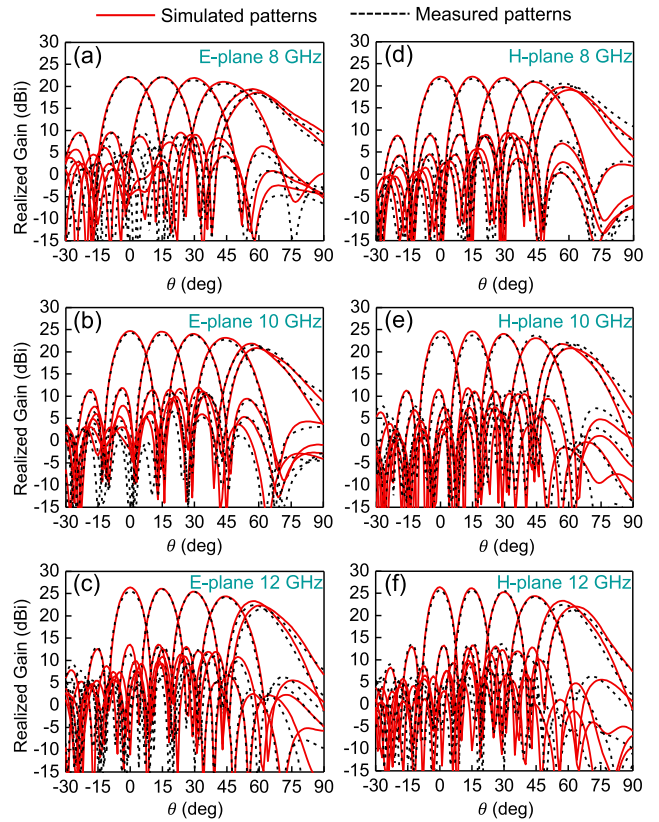


FIGURE 21. Measured and simulated radiation patterns for 0°, 15°, 30°, 45°, 60° and 65° scans in the principal planes. (a) E-plane @ 8 GHz; (b) E-plane @ 10 GHz; (c) E-plane @ 12 GHz; (d) H-plane @ 8 GHz; (e) H-plane @ 10 GHz; (f) H-plane @ 12 GHz.

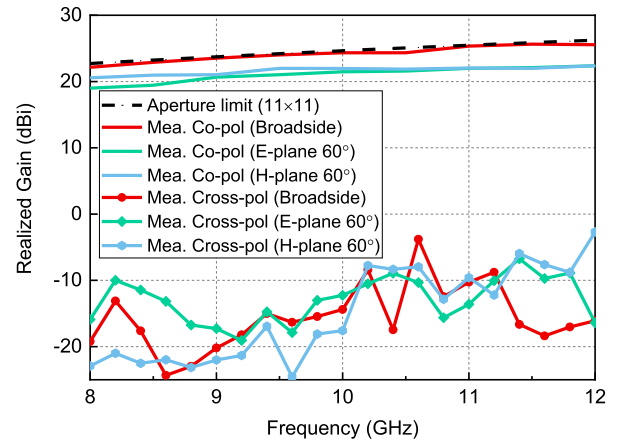


FIGURE 22. Measured co-polarized and cross-polarized realized gains of the prototype array at broadside and 60° scan in the E- and H-planes, along with the theoretical aperture limits.

along with the theoretical gain limits for the total aperture. The ideal aperture limit is calculated using $4\pi A/\lambda_0^2$, where A is the aperture area, and λ_0 is the wavelength in free space. The dashed black curve is the total aperture limit of the 11×11 array. The measured broadside co-polarized gains (solid red curve) are very close to the total aperture limits, which indicates a high aperture efficiency. Compared

with the broadside co-polarized gains, the largest gain drop at 60° scan in both E- and H-planes is less than 3.5 dB across the entire frequency band. The proposed array has good cross-polarization characteristic. The simulated cross-polarized gains are too low, which are not plotted in Fig. 22. The measured cross-polarized gains of the array at broadside and 60° scan in the E- and H-planes remain at least 25 dB lower than the corresponding co-polarized gains within the operating band, as shown in Fig. 22. The measured higher cross-polarized gains result from the measurement precision limit of the anechoic chamber and the misalignments of the array and the feeding horns.

IV. CONCLUSION

This paper presents a wideband wide-scanning open-ended rectangular waveguide phased array in the triangular lattice. The infinite array achieves 40% bandwidth (8-12 GHz) with VSWR < 2 while scanning to 60° in the E-plane and 65° in the H-plane. The scan blindnesses caused by the surface wave are displayed in the active reflection coefficient spectrums and active element patterns clearly. The scan blindness free design of the proposed array has been studied in detail. The proposed modulated surface structures, which consist of pyramidal dielectric protrusions and tapered metallic walls, contribute to achieving optimal scanning performance over the whole desired frequency band (from the waveguide TE₁₀ cutoff frequency to the onset frequency of the first grating lobe). The tapered metallic walls are utilized to construct broad surface wave bandgaps in both E- and H-planes, thus eliminating the scan blindnesses in the operating frequency band. The pyramidal dielectric protrusions are employed as a WAIM layer to maintain good impedance matching during the beam scanning. A coaxial-to-rectangular waveguide transition with more than 40% bandwidth is designed to feed each array element. An 11×11 single-polarized prototype array is fabricated and measured to validate the design. The realized gains and radiation patterns show good agreement with simulations. The measured results for the proposed array show cross-polarization levels less than -25 dB over the whole operating band at broadside and 60° scan in both E- and H-planes. The merits of wideband, large scan volume, compact size and stable structure make the array an excellent candidate for various applications. It is worth noting that the proposed waveguide array with feeding structures has a relatively high profile, and it is kind of like Vivaldi array in shape. While compared with the Vivaldi phased arrays, the proposed design can be easily extended to a coincident phase center circularly polarized array by using the circular polarizer.

REFERENCES

- [1] D. Manteuffel and R. Martens, "Compact multimode multielement antenna for indoor UWB massive MIMO," *IEEE Trans. Antennas Propag.*, vol. 64, no. 7, pp. 2689–2697, Jul. 2016.
- [2] S. J. Wijnholds, W. A. van Cappellen, J. G. B. de Vaate, and A. van Ardenne, "Phased-array antenna system development for radio-astronomy applications," *IEEE Antennas Propag. Mag.*, vol. 55, no. 6, pp. 293–308, Dec. 2013.
- [3] J. D. Diaz, J. L. Salazar, J. A. Ortiz, C. Fulton, N. Aboserwal, R. Kelley, and R. Palmer, "A dual-polarized cross-stacked patch antenna with wide-angle and low cross-polarization for fully digital multifunction phased array radars," in *Proc. IEEE Int. Symp. Phased Array Syst. Technol. (PAST)*, Waltham, MA, USA, Oct. 2016, pp. 1–4.
- [4] R. Mailloux, *Phased Array Antenna Handbook*, 2nd ed. Norwood, MA, USA: Artech House, 2005.
- [5] D. Pozar and D. Schaubert, "Scan blindness in infinite phased arrays of printed dipoles," *IEEE Trans. Antennas Propag.*, vol. AP-32, no. 6, pp. 602–610, Jun. 1984.
- [6] A. K. Bhattacharyya, *Phased Array Antennas: Floquet Analysis Synthesis in BFNs and Active Array Systems*. Hoboken, NJ, USA: Wiley, 2006.
- [7] J. Allen, "On surface-wave coupling between elements of large arrays," *IEEE Trans. Antennas Propag.*, vol. AP-13, no. 4, pp. 638–639, Jul. 1965.
- [8] G. Farrell and D. Kuhn, "Mutual coupling in infinite planar arrays of rectangular waveguide horns," *IEEE Trans. Antennas Propag.*, vol. AP-16, no. 4, pp. 405–414, Jul. 1968.
- [9] G. H. Knittel, A. Hessel, and A. A. Oliner, "Element pattern nulls in phased arrays and their relation to guided waves," *Proc. IEEE*, vol. 56, no. 11, pp. 1822–1836, Nov. 1968.
- [10] H. Koo and S. Nam, "Mechanism and elimination of scan blindness in a T-printed dipole array," *IEEE Trans. Antennas Propag.*, vol. 68, no. 1, pp. 242–253, Jan. 2020.
- [11] R. B. Waterhouse, "Improving the scan performance of probe-fed microstrip patch arrays on high dielectric constant substrates," *IEEE Trans. Antennas Propag.*, vol. 43, no. 7, pp. 705–712, Jul. 1995.
- [12] D. H. Schaubert, "A class of E-plane scan blindnesses in single-polarized arrays of tapered-slot antennas with a ground plane," *IEEE Trans. Antennas Propag.*, vol. 44, no. 7, pp. 954–959, Jul. 1996.
- [13] A. Ellgardt, "A scan blindness model for single-polarized tapered-slot arrays in triangular grids," *IEEE Trans. Antennas Propag.*, vol. 56, no. 9, pp. 2937–2942, Sep. 2008.
- [14] Z. Xu, C. Zhang, T. Kaufmann, X. Yan, Y. Yuan, and C. Fumeaux, "Analysis of scan blindness in a linearly polarized tapered-slot phased array in triangular lattice—Performance improvement with parasitic notches," *IEEE Trans. Antennas Propag.*, vol. 62, no. 8, pp. 4057–4066, Aug. 2014.
- [15] D. M. Pozar, "Scanning characteristics of infinite arrays of printed antenna subarrays," *IEEE Trans. Antennas Propag.*, vol. 40, no. 6, pp. 666–674, Jun. 1992.
- [16] R. Mailloux, "On the use of metallized cavities in printed slot arrays with dielectric substrates," *IEEE Trans. Antennas Propag.*, vol. AP-35, no. 5, pp. 477–487, May 1987.
- [17] M. H. Awida, A. H. Kamel, and A. E. Fathy, "Analysis and design of wide-scan angle wide-band phased arrays of substrate-integrated cavity-backed patches," *IEEE Trans. Antennas Propag.*, vol. 61, no. 6, pp. 3034–3041, Jun. 2013.
- [18] D.-B. Hou, S. Q. Xiao, B.-Z. Wang, L. Jiang, J. Wang, and W. Hong, "Elimination of scan blindness with compact defected ground structures in microstrip phased array," *IET Microw., Antennas Propag.*, vol. 3, no. 2, pp. 269–275, Mar. 2009.
- [19] L. Zhang, J. A. Castaneda, and N. G. Alexopoulos, "Scan blindness free phased array design using PBG materials," *IEEE Trans. Antennas Propag.*, vol. 52, no. 8, pp. 2000–2007, Aug. 2004.
- [20] E. Adas, F. De Flaviis, and N. G. Alexopoulos, "Realization of scan blindness free finite microstrip phased arrays based on mode-free radiating electromagnetic bandgap materials," *IEEE Trans. Antennas Propag.*, vol. 66, no. 7, pp. 3375–3382, Jul. 2018.
- [21] L. Li, C.-H. Liang, and C.-H. Chan, "Waveguide end-slot phased array antenna integrated with electromagnetic bandgap structures," *J. Electromagn. Waves Appl.*, vol. 21, no. 2, pp. 161–174, Jan. 2007.
- [22] S. P. Skobelev and P.-S. Kildal, "Blindness removal in arrays of rectangular waveguides using dielectrically loaded hard walls," *IEEE Trans. Antennas Propag.*, vol. 46, no. 4, pp. 546–550, Apr. 1998.
- [23] H. Wheeler, "Simple relations derived from a phased-array antenna made of an infinite current sheet," *IEEE Trans. Antennas Propag.*, vol. AP-13, no. 4, pp. 506–514, Jul. 1965.
- [24] E. Magill and H. Wheeler, "Wide-angle impedance matching of a planar array antenna by a dielectric sheet," *IEEE Trans. Antennas Propag.*, vol. AP-14, no. 1, pp. 49–53, Jan. 1966.
- [25] H. van Schaik, "The performance of an iris-loaded planar phased-array antenna of rectangular waveguides with an external dielectric sheet," *IEEE Trans. Antennas Propag.*, vol. AP-26, no. 3, pp. 413–419, May 1978.

- [26] T. R. Cameron and G. V. Eleftheriades, "Analysis and characterization of a wide-angle impedance matching metasurface for dipole phased arrays," *IEEE Trans. Antennas Propag.*, vol. 63, no. 9, pp. 3928–3938, Sep. 2015.
- [27] S. Sajuyigbe, M. Ross, P. Geren, S. A. Cummer, M. H. Tanielian, and D. R. Smith, "Wide angle impedance matching metamaterials for waveguide-fed phased-array antennas," *IET Microw., Antennas Propag.*, vol. 4, no. 8, pp. 1063–1072, Aug. 2010.
- [28] A. B. Smolders, "Design and construction of a broadband wide-scan angle phased-array antenna with 4096 radiating elements," in *Proc. IEEE Int. Symp. Phased Array Syst. Technol. (PAST)*, Boston, MA, USA, Oct. 1996, pp. 87–92.
- [29] C. C. Chen, "Wideband wide-angle impedance matching and polarization characteristics of circular waveguide phased arrays," *IEEE Antennas Propag. Mag.*, vol. AP-22, no. 3, pp. 4188–4414, May 1974.
- [30] L. Lewis, A. Hessel, and G. Knittel, "Performance of a protruding-dielectric waveguide element in a phased array," *IEEE Trans. Antennas Propag.*, vol. AP-20, no. 6, pp. 712–722, Nov. 1972.
- [31] B. E. Grann, M. G. Moharam, and A. P. Drew, "Optimal design for antireflective tapered two-dimensional subwavelength grating structures," *J. Opt. Soc. Amer. A, Opt. Image Sci.*, vol. 12, no. 2, pp. 333–339, Feb. 1995.
- [32] K. Q. Zhang and D. J. Li, *Electromagnetic Theory for Microwaves and Optoelectronics*, 2nd ed. Berlin, Germany: Springer, 2008.
- [33] G. Oliveri, M. Salucci, N. Anselmi, and A. Massa, "Multiscale system-by-design synthesis of printed WAIMs for waveguide array enhancement," *IEEE J. Multiscale Multiphys. Comput. Techn.*, vol. 2, pp. 84–96, May 2017.
- [34] Y. Zhou, E. Li, G.-F. Guo, T. Yang, and L.-S. Liu, "Design of millimeter wave wideband transition from double-ridge waveguide to coaxial line," *J. Infr., Millim., THz Waves*, vol. 32, no. 1, pp. 26–33, Jan. 2011.
- [35] D. M. Pozar, "The active element pattern," *IEEE Trans. Antennas Propag.*, vol. 42, no. 8, pp. 1176–1178, Sep. 1994.



XIUYE LIANG (Student Member, IEEE) was born in Handan, Hebei, China, in 1993. He received the B.S. degree in optoelectronic information science and engineering from Jiangnan University, Wuxi, China, in 2016. He is currently pursuing the Ph.D. degree with Fudan University, Shanghai, China.

His current research interests include phased array feed antennas, ultrawideband phased arrays, artificial bandgap materials, and artificial intelligence in antenna design.



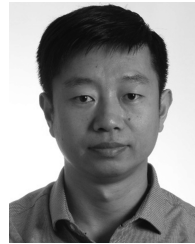
ZHE ZHANG was born in Tianjin, China, in 1995. He received the B.S. degree from the School of Physics, Dalian University of Technology, Dalian, China, in 2017. He is currently pursuing the Ph.D. degree with Fudan University, Shanghai, China.

His current research interests include phased array antennas, frequency selective surface, and artificial bandgap materials.



JIANPING ZENG (Graduate Student Member, IEEE) was born in Ruijin, Jiangxi, China. He received the B.S. degree in applied physics from Jiangxi Normal University, in 2018. He is currently pursuing the Ph.D. degree with Fudan University.

His current research interests include wideband antennas, analysis and design of antennas using characteristic mode theory, reconfigurable antennas, and phased array antennas.



FANG GUAN was born in Yixian, Liaoning, China, in 1979. He received the B.S. degree in applied physics and the M.S. and Ph.D. degrees in condensed matter physics from Fudan University, China, in 2002, 2005, and 2014, respectively.

From 2014 to 2019, he was a Research Assistant with the Department of Physics, Fudan University. He is currently an Associate Professor with the Institute for Nanoelectronic Devices and Quantum Computing, Fudan University. His research interests include photonic crystals, metasurfaces, phased arrays, and ultrawideband antenna arrays.



XIAOHAN LIU was born in Jiangsu, China. He received the B.S., master's, and Ph.D. degrees from Fudan University, in 1993, 1996, and 1999, respectively.

From 2003 to 2007, he was a Lecturer with the Department of Physics, Fudan University, and held a postdoctoral position with the University of Munster, Germany. From 2007 to 2012, he was an Associate Professor with the Department of Physics, Fudan University. Since 2012, he has been a Professor with the Department of Physics, Fudan University. He has authored or coauthored more than 100 technical articles. His current research interests include optical properties of condensed matter, photonic crystals, and array antenna.



JIAN ZI was born in Sichuan, China. He received the B.S., master's, and Ph.D. degrees from Fudan University, in 1985, 1988, and 1991, respectively.

From 1991 to 1995, he was a Lecturer with the Department of Physics, Fudan University, and held a postdoctoral position with the University of Munster, Germany. From 1994 to 1995, he was an Associate Professor with the Department of Physics, Fudan University. Since 1996, he has been a Professor with the Department of Physics, Fudan University, and access to the National Science Fund for Distinguished Young Scholars. He has been a Chang-Jiang Professor nominated by the Ministry of Education of China, since 2001. He was appointed as the Chief Scientist of project 973 by the Ministry of Science and Technology, in 2001 and 2007. He has authored or coauthored over 300 technical articles. His current research interests include photonic crystals, plasmonics, metamaterials, natural photonic structures and structural colors, and liquid surface waves propagating in periodic structures.

...